Additive Manufacturing Letters 3 (2022) 100086

Contents lists available at ScienceDirect

Additive Manufacturing Letters

journal homepage: www.elsevier.com/locate/addlet

Using θ' interfaces as templates for planar $L1_2$ precipitation in AlCuMnZr alloys ☆

Jonathan D. Poplawsky[a,*], Richard A. Michi[b], Lawrence F. Allard[b], Sumit Bahl[b], Alex J. Plotkowski[b], Amit Shyam[b,*]

[a] Center for Nanophase Materials Sciences, Oak Ridge National Laboratory, Oak Ridge, TN
[b] Materials Science and Technology Division, Oak Ridge National Laboratory, Oak Ridge, TN

ARTICLE INFO

Keywords:
Aluminum alloy
Precipitate stability
Elemental diffusion
Atom probe tomography
Scanning transmission electron microscopy

ABSTRACT

Controlled Mn and Zr additions to Al-Cu alloys have allowed for the improved retention of mechanical properties after extended 350°C exposures by stabilizing the main strengthening θ' (Al_2Cu) phase. Ultimately, θ'/$L1_2$ (Al_3Zr) co-precipitate formation stabilizes θ' most effectively; however, Zr diffuses sluggishly and has low solubility in aluminum castings. Increasing the Zr segregation rate would allow for faster and more effective θ'/$L1_2$ co-precipitation. It is demonstrated that the Zr segregation rate is faster when the Zr matrix content is higher. A much higher Zr matrix content was achieved by rapid cooling during additive manufacturing (AM) that produces θ'/$L1_2$ co-precipitation faster, which is shown by scanning transmission electron microscopy and atom probe tomography experiments. It was also found that Zr continuously segregates to θ' interfaces up to the most aggressive heat treatment studied such that planar $L1_2$ precipitates remain after the metastable θ' dissolves. In this manner, we demonstrate that θ' coherent interfaces serve as perfect templates to form stable planar $L1_2$ precipitates that can provide strength at higher temperatures than traditional θ' strengthened AlCu alloys. This work introduces an alloy design strategy that uses metastable precipitates to quickly nucleate and grow co-precipitates with a desired geometry that contain slow diffusing elements. These ideas can be applied to engineer more heat resistant alloys by taking advantage of high solute matrix contents enabled by rapid cooling during additive manufacturing.

Introduction

Increasing the operating temperature of lightweight Al alloys can enable more fuel-efficient internal combustion engines (ICEs) and can reduce weight in regenerative braking systems for electric vehicles (EVs). Al-Cu and Al-Cu-Si alloys have been widely used in ICE applications because they are castable, strong, and affordable [1–4]. The strength from these alloys results from a matrix populated with a high number density of high-aspect-ratio θ' precipitates (Al_2Cu) [5]. The θ' phase often manifests as a high-aspect-ratio octagonal prism-shaped precipitate with 2 coherent interfaces (CIs) in the (001) plane, 4 semi-coherent interfaces (SCIs) in the (001) plane, and 4 SCIs in the (110) plane [6]. θ' precipitates, however, are thermodynamically metastable and transform into coarse, low-aspect-ratio θ precipitates (Al_2Cu) above approximately 250°C [7]. The SCI has a much higher interfacial energy of ~ 500 mJ/m^2 than the CI (200 mJ/m^2), and therefore, is the least stable interface [8]. Reducing interfacial energy through solute segregation and creating a θ'/$L1_2$ co-precipitate structure has recently been demonstrated to stabilize θ' precipitates to higher temperatures [4, 9-13], which is a concept similar to other core-shell structured precipitates in Al and Ni-based superalloys [14–18].

Mn, Zr, Ti, Fe, and Sc are microalloying elements that segregate to θ' interfaces and improve their thermal stability [4, 9-13]. Sc, Zr, and Ti additions segregate to the θ'-CIs forming θ'/$L1_2$ co-precipitates. Sc is the fastest diffusing trialuminide former and can segregate to θ'-CIs to delay the θ'/ θ transformation, while Ti and Zr are slow diffusers and require additional θ' stabilization for their effective segregation [19–21]. Mn additions provide for this intermediate stabilization. The faster diffusing Mn segregates to CIs and SCIs stabilizing θ' to 300°C, which allows for Ti and Zr to form θ'/$Al_3(Zr_xTi_{1-x})$ co-precipitates at the CI that stabilizes θ' to 350°C [6]. Interestingly, Zr continues to segregate to θ' up to the

☆ This manuscript has been authored by UT-Battelle, LLC, under contract DE-AC05-00OR22725 with the US Department of Energy (DOE). The US government retains and the publisher, by accepting the article for publication, acknowledges that the US government retains a nonexclusive, paid-up, irrevocable, worldwide license to publish or reproduce the published form of this manuscript, or allow others to do so, for US government purposes. DOE will provide public access to these results of federally sponsored research in accordance with the DOE Public Access Plan (http://energy.gov/downloads/doe-public-access-plan).

* Corresponding authors at: 1 Bethel Valley Rd., Oak Ridge, TN 37831
E-mail addresses: poplawskyjd@ornl.gov (J.D. Poplawsky), shyama@ornl.gov (A. Shyam).

https://doi.org/10.1016/j.addlet.2022.100086
Received 15 June 2022; Received in revised form 18 July 2022; Accepted 5 August 2022
Available online xxx

Table 1
Measured composition of cast and AM-ACMZ alloys by ICP-OES. Wt.% and at.% values are displayed.

Alloy	Al	Cu	Mn	Zr	Si	Fe	Zn	Ni	Ti
AM-ACMZ (wt.)	89.9	8.6	0.45	0.9	0.06	0.09	-	-	-
cast-ACMZ (wt.)	93.03	6.4	0.19	0.13	0.01	0.1	0.04	0.01	0.09
AM-ACMZ (at.)	95.50	3.88	0.23	0.28	0.06	0.05	-	-	-
cast-ACMZ (at.)	96.90	2.83	0.10	0.04	0.01	0.05	0.02	0.00	0.05

most extreme heat treatment in a previous study (350°C for 5,000h) [6]. Density functional theory (DFT) calculations have shown that the θ'-CI /Al_3Zr interface has a near zero interfacial energy compared to the 200 mJ/m^2 θ'-CI/α-Al interface, which drives Zr to segregate at that interfacial location [8].

An additively manufactured version of Al-Cu-Mn-Zr (AM-ACMZ) alloy was recently fabricated [22]. AM-ACMZ has refined microstructural features, such as a bimodal micron-scale grain structure and nanoscale θ intermetallic particles that form during non-equilibrium eutectic solidification. These features lead to both improved strength and tensile elongation compared to cast-ACMZ.

Rapid solidification during the AM process is another advantage of AM-ACMZ that leads to the matrix becoming supersaturated in solute elements, such as Zr [23–27]. A matrix supersaturated in Zr allows for spherical Al_3Zr $L1_2$ nanoprecipitate nucleation and growth with a high number density and volume fraction. In addition, θ'/$L1_2$ co-precipitates formed after a relatively short thermal exposure (300°C, 200h), which was only found in cast-ACMZ after extended exposures to 350°C [6, 27]. Strengthening for cast-ACMZ is primarily from θ' precipitates, while AM-ACMZ is strengthened by a complex microstructure containing θ', eutectic θ, and spherical Al_3Zr-$L1_2$ precipitates with fewer coarser θ precipitates in the melt pool boundaries compared to the melt pool interior as a result of different solidification rates [27]. The complex microstructure of AM-ACMZ suppresses θ' precipitation with only 0.2 vol.% of that phase in the as-printed version compared to 2.8 vol% in cast-ACMZ after solutionizing and aging the alloy [28, 29]. Previous AM-ACMZ studies were primarily focused on understanding microstructure/mechanical property relationships, such as linking $L1_2$, θ', and θ precipitate size and number density to strength. These studies did not systematically investigate solute segregation rates to θ' interfaces or $L1_2$/θ' co-precipitate formation within AM-ACMZ [22, 27]. Understanding the mechanistic commonalities and differences of solute segregation to θ' interfaces in cast versus additively processed microstructures is the motivation behind the present study.

The θ' microstructure, interfacial θ' solute segregation behaviors, and $L1_2$/θ' co-precipitate formation are compared in cast and AM-ACMZ using high-angle annular dark-field (HAADF) scanning transmission electron microscopy (STEM) and atom probe tomography (APT). The results presented in this study show that Zr segregation rates to precipitate interfaces are faster in the AM alloy due to the higher matrix Zr content. Also, Zr is shown to continuously segregate to $L1_2$ precipitates at θ'-CIs, and planar $L1_2$ precipitates remain after θ' dissolves. The information presented here can be used to develop new AM based alloy design strategies to increase the thermal stability of θ' as well as use metastable precipitates as templates to form desired stable precipitate geometries [30].

Materials and methods

Alloy fabrication

The processing procedure for the AM-ACMZ alloy is described in detail by Shyam *et al.* [22]. Briefly, this alloy was fabricated by laser powder bed fusion (LPBF) with a 370 W laser power, 1300 mm s^{-1} laser speed, a 95 µm laser spot size, 0.15 mm hatch spacing, a 30 µm layer thickness, and 200°C preheat temperature. A full description of the fabrication process for cast-AMCZ is described by Shyam *et al.* [4]. The chemical compositions of the studied alloys determined using inductively coupled plasma optical emission spectroscopy (ICP-OES) are given in Table 1. The 7x higher Zr content in AM-ACMZ compared to cast-ACMZ was inspired by previously published AM Al alloys, and was done to improve processability and supersaturate the matrix with Zr, which is only possible in the AM alloy due to rapid solidification during the additive process [23, 24].

Microscopy sample preparation and data analysis

Electron-transparent thin-foil specimens for STEM imaging were prepared using standard slicing, grinding, and electropolishing methods (e.g., Struers Tenupol dual-jet system). HAADF- STEM images were obtained using an aberration-corrected (CEOS GmbH, Heidelberg) JEOL 2200FS instrument. Additional details are provided elsewhere [4].

APT specimens were fabricated using standard lift-out and sharpening methods as described by Thompson *et al.* using a Thermo Fisher Nova 200 Dual Beam scanning electron microscope/focused ion beam (SEM/FIB) [31]. APT needles were fabricated from both melt pool boundaries and melt pool interiors. The APT experiments were run using a CAMECA LEAP 4000XHR in voltage mode with a 70K base temperature, 20-30% pulse fraction, and a 0.5% detection rate. The APT results were reconstructed and analyzed using CAMECA's interactive

Table 2
The matrix Cu, Mn, Zr, and Si contents (in at.%) for different heat treatments for AM-ACMZ as measured by APT. The reported values are an average of several APT datasets (# needles) and the error is the standard deviation. The Zr diffusion distance is calculated using the expression $x = \sqrt{6Dt}$, where x is the mean diffusion distance, D is the diffusivity of Zr in pure Al using the parameters in Knipling *et al.* [19], and t is the diffusion time. D was calculated using the Arrhenius equation ($D = D_o e^{-E_A/RT}$), where D_o is the maximal diffusion coefficient (7.18×10^{-2} $m^2 s^{-1}$ for Zr), E_A is the activation energy for diffusion (242 kJ mol^{-1} for Zr), T is the absolute temperature, and R is the universal gas constant.

Heat Treatment	# needles	Zr diff. distance (nm)	Matrix Cu	Matrix Mn	Matrix Zr	Matrix Si
As-fabricated	6	0	0.39 ± 0.17	0.16 ± 0.03	0.30 ± 0.03	0.012 ± 0.003
300°C, 200 h	8	5.5	0.18 ± 0.01	0.13 ± 0.07	0.10 ± 0.03	0.006 ± 0.005
300°C, 573 h	4	8.9	0.16 ± 0.07	0.02 ± 0.01	0.02 ± 0.01	0.003 ± 0.001
350°C, 24 h	7	8.5	0.33 ± 0.03	0.09 ± 0.03	0.06 ± 0.02	0.001 ± 0.004
350°C, 220 h	5	42.1	0.37 ± 0.01	0.02 ± 0.01	0.04 ± 0.01	0.003 ± 0.006

Table 3
The matrix Cu, Mn, Zr, and Si contents for different heat treatments within cast-ACMZ as measured by APT. The lower matrix Cu content for the 350°C, 850 h heat treatment could be due to localized effects because the APT needles were taken from an approximately 10 μm region of interest within one grain. The reported values are an average of several APT datasets (# needles) and the error is the standard deviation. The Zr diffusion distance calculation is described in Table 2's caption.

Heat Treatment	# needles	Zr diff. distance (nm)	Matrix Cu	Matrix Mn	Matrix Zr	Matrix Si
As-aged	9	0	0.15 ± 0.03	0.10 ± 0.02	0.04 ± 0.00	0.04 ± 0.01
300°C, 200 h	12	5.2	0.19 ± 0.03	0.06 ± 0.02	0.03 ± 0.01	0.02 ± 0.01
300°C, 1524 h	7	14.3	0.15 ± 0.03	0.07 ± 0.03	0.02 ± 0.01	0.02 ± 0.01
300°C, 2113 h	9	17.0	0.20 ± 0.02	0.05 ± 0.03	0.02 ± 0.00	0.03 ± 0.01
300°C, 5014 h	9	26.2	0.20 ± 0.03	0.07 ± 0.03	0.01 ± 0.01	0.01 ± 0.01
350°C, 200 h	5	40.2	0.38 ± 0.05	0.06 ± 0.02	0.03 ± 0.01	0.02 ± 0.01
350°C, 850 h	5	82.8	0.14 ± 0.02	0.03 ± 0.01	0.01 ± 0.00	0.00 ± 0.00
350°C, 2000 h	9	127.0	0.38 ± 0.05	0.05 ± 0.03	0.02 ± 0.00	0.03 ± 0.01
350°C, 5000 h	4	200.9	0.31 ± 0.04	0.07 ± 0.03	0.01 ± 0.01	0.01 ± 0.01

visualization and analysis software (IVAS 3.8). Interfacial composition profiles are proximity histograms using a 10 at. % Cu isoconcentration surface from isolated regions of interest only containing coherent (C) or semi-coherent (SC) interfaces. Manual background subtraction was performed for Mn, Zr, and Ti by subtracting background immediately before and after the mass spectral peaks encompassing a similar time window as the peaks themselves. The APT calculated matrix compositions for AM and cast-ACMZ subject to different heat treatments are shown in Tables 2 and 3, respectively.

Results

Scanning transmission electron microscopy

As-aged cast-ACMZ and as-printed AM-ACMZ HAADF-STEM images are displayed in Fig. 1a and d. There are two distinct differences in θ' precipitate characteristics between these two microstructures: (1) cast-ACMZ contains larger mean diameter θ' precipitates than AM-ACMZ (~275 nm vs ~130 nm) with similar precipitate thicknesses (~7-8 nm)

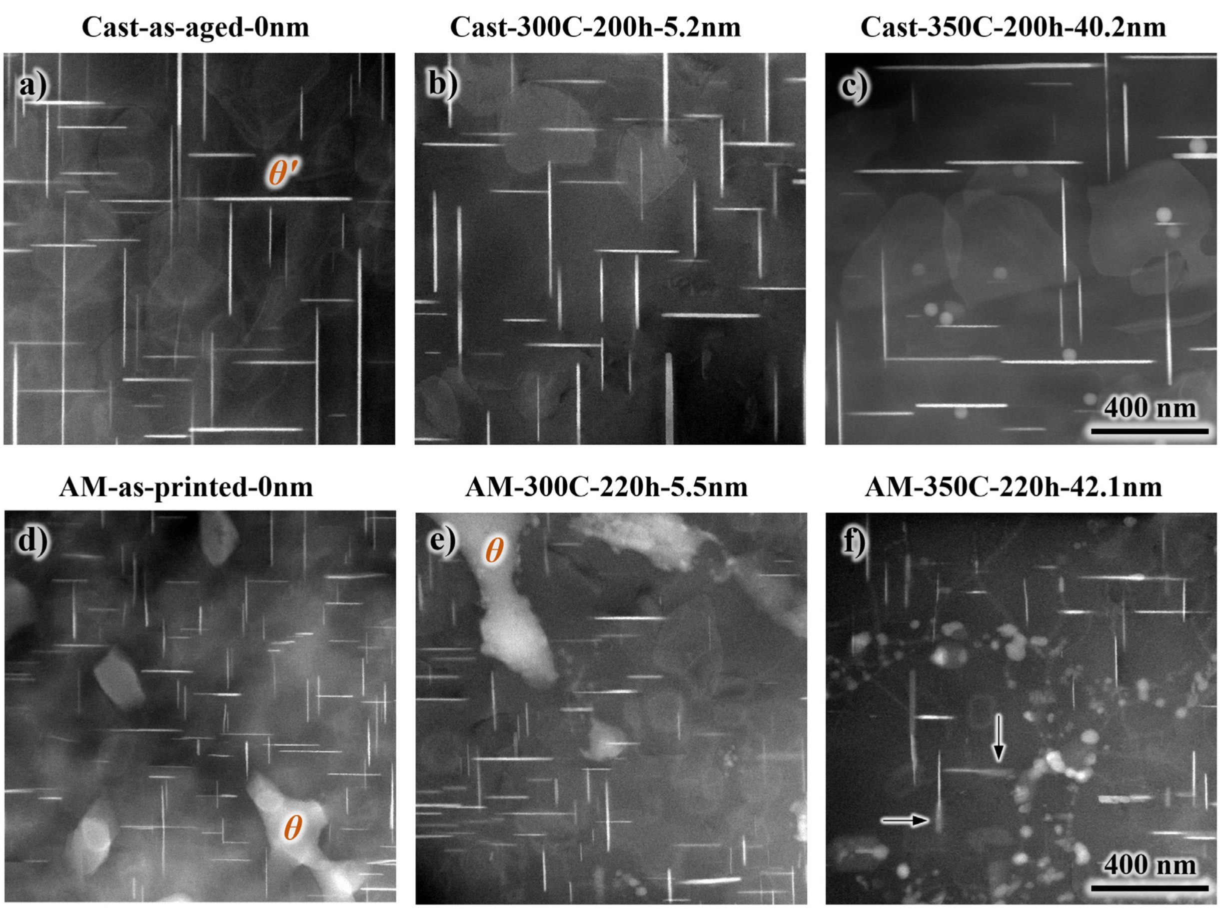

Fig. 1. STEM-HAADF images of the nanostructure in (a-c) cast and (d-f) AM-ACMZ in the (a) as-aged and (d) as printed states and after (b) 300°C, 200h, (c) 350°C, 200h, (e) 300°C, 220h, and (f) 350°C, 220h heat treatments. All images have the same magnification. The arrows in f show examples of Cu diffusing out of θ'. The distances displayed on top of the images are the Zr diffusion distances induced by the corresponding heat treatment as calculated using the equations in Table 2.

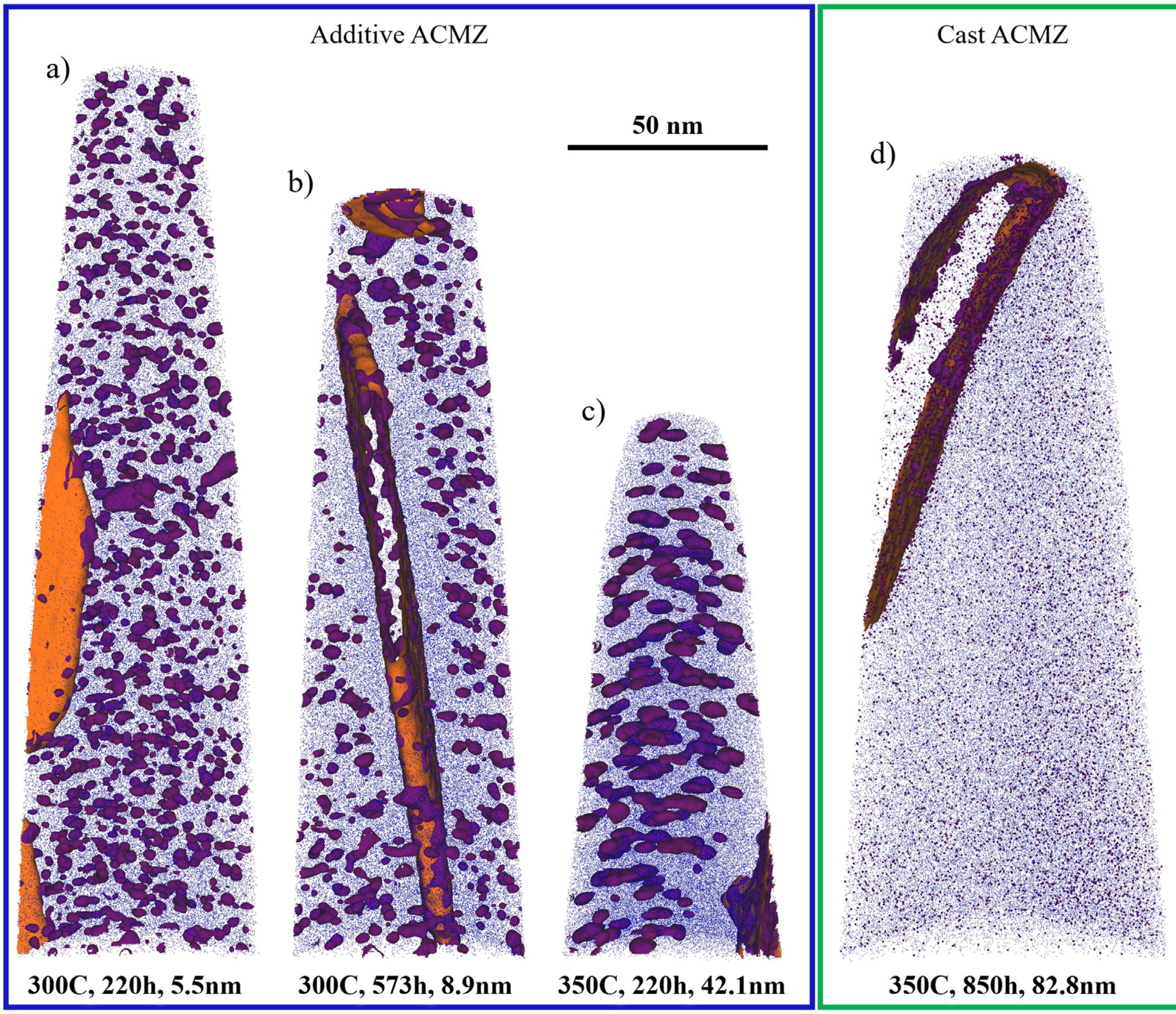

Fig. 2. Al and Zr APT atom maps of AM and cast-ACMZ with 10 at.% Cu (orange) and 2 at.% Zr (purple) isoconcentration surfaces revealing θ' and $L1_2$ precipitates, respectively. All images are the same magnification. The values reported below the APT datasets are the heat treatment conditions followed by the diffusion distance calculated using the expression $x = \sqrt{6Dt}$ (see Table 2 caption for more details).

and (2) θ' is on average in closer proximity to θ in AM-ACMZ [27, 28]. Large θ' precipitate size and spacing positively correlates with thermal stability, while θ inhibits θ' stability when in close proximity to θ' as large θ' precipitation-free zones (PFZ) around θ precipitates were previously observed [32–34]. These observations are linked to better inherent θ' coarsening resistance in cast-ACMZ compared to AM-ACMZ; however, the higher Zr content (a θ' stabilizer) in the AM-ACMZ matrix could negate these effects.

STEM images reveal that there is no noticeable coarsening in the cast or AM-ACMZ after 300°C aging, while there are visible differences in the microstructures after 350°C aging. For cast-ACMZ, there appear to be a lower number density of longer θ' precipitates, while for AM-ACMZ, the θ' size and morphology appear to be the same, but their number density and volume fraction decrease. This observation along with the bright streaks coming out of the θ'-SCIs suggest that Cu from θ' is dissolving into the matrix (arrows in Fig. 1f). Interestingly, residual planar Al_3Zr $L1_2$ precipitates where θ' precipitates existed before dissolution were also observed (see Supplementary Fig. 1). This scenario is evidence that Al_3Zr $L1_2$ formation on the θ'-CIs pins these interfaces and prevents coarsening, while the proximity to θ aides the dissolution of θ' precipitates as θ can quickly consume the dissolved Cu.

Atom probe tomography

APT experiments reveal the solute segregation behaviors to θ' interfaces, spacing between spherical $L1_2$ in AM-ACMZ, and the $L1_2$ PFZ in proximity to θ'. More details regarding spherical $L1_2$ nucleation, growth, and coarsening are published elsewhere [27]. Fig. 2 displays APT atom maps for AM and cast-ACMZ with 2 at.% Zr and 10 at.% Cu isoconcentration surfaces revealing $L1_2$ and θ' precipitates, respectively. A high number-density of spherical $L1_2$ precipitates is formed in AM-ACMZ after a 220h, 300°C heat-treatment. After 573h at 300°C, the inter-precipitate distance and PFZ size are ~20-50 nm and ~20 nm, respectively. The cast-ACMZ sample does not show small spherical $L1_2$ particles embedded in the matrix for any heat treatment condition; however, $L1_2$ precipitation on the θ'-CIs is present. $L1_2$ precipitation is also found on the θ'-SCIs, which has yet to be observed in cast-ACMZ [6, 27].

θ'-CI concentration profiles are displayed in Fig. 3. The results reveal that more Zr segregates to θ'-CIs in AM-ACMZ than cast-ACMZ for all aging conditions. The Mn segregation behavior is found to be the same for AM-ACMZ and cast-ACMZ after the ~200h at 300°C exposure, while, after a ~200h at 350°C exposure, Mn does not segregate to θ'-CIs in AM-ACMZ unlike the segregation behavior in cast-ACMZ. The lack of

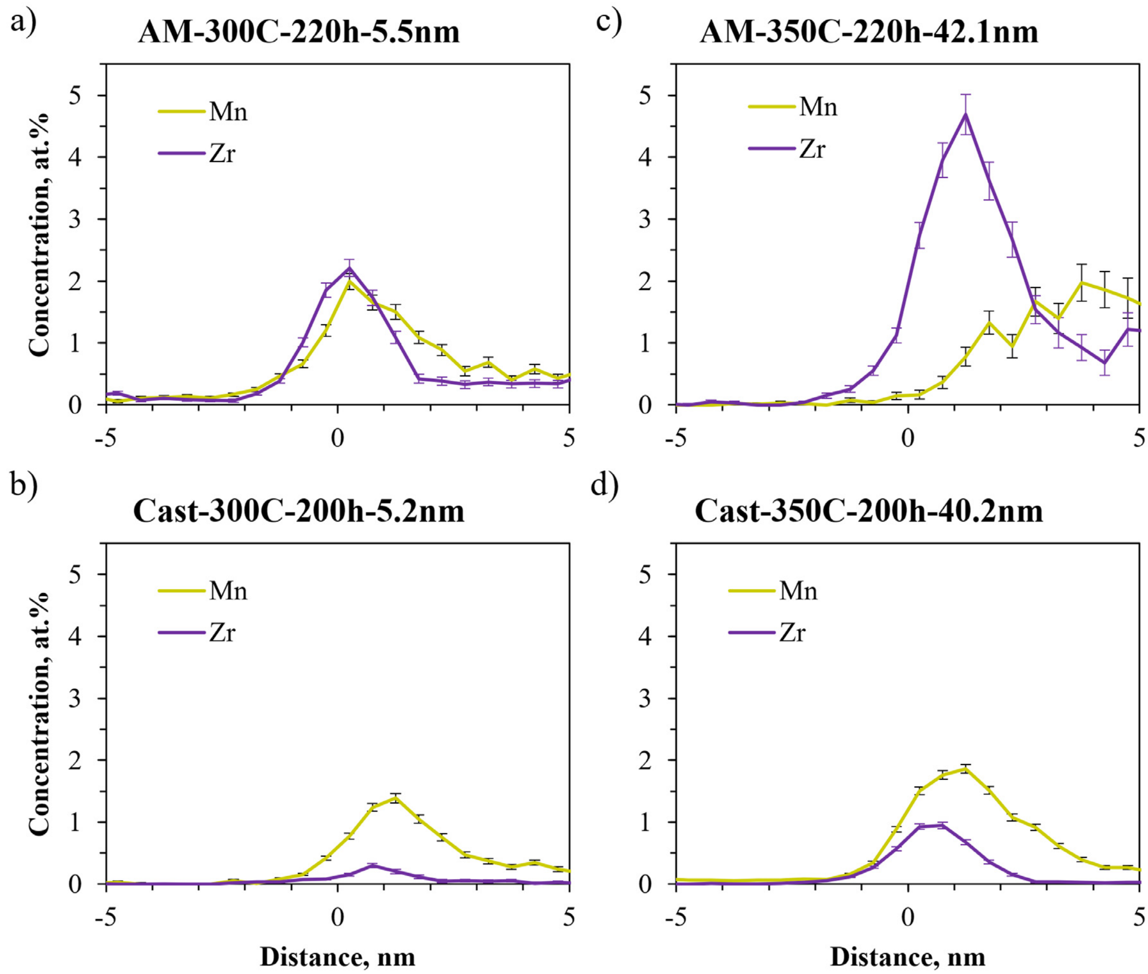

Fig. 3. θ-CI concentration profiles created using proximity histograms from 10 at.% Cu isoconcentration surfaces within the APT data revealing Mn and Zr θ'-CI segregation profiles for (a) AM-ACMZ after 220h, 300°C, (b) cast-ACMZ after 200h, 300°C, (c) AM-ACMZ after 220h, 350°C, and (d) cast-ACMZ after 200h, 350°C heat-treatments. The θ'-CIs were isolated from the SC interfaces before creating the proximity histograms. Although there are Al_3Zr precipitates at the interface, less than 25 at. % Zr was measured in these profiles. This is due to APT's interfacial resolution limits and/or a non-uniform $L1_2$ structure at the interface as shown in Figs. 2a and 5 of Poplawsky *et al.* [6]. The resolution limit causes mixing of the matrix, $L1_2$, and θ' compositions and reduce the overall Zr content. These graphs with the Cu concentration profiles included (showing the interface location) can be found in Supplementary Fig. 3. The displayed distances in the graph titles are the diffusion distances calculated using the method described in the caption of Table 2.

Mn segregation for AM-ACMZ is most likely linked to $L1_2$ precipitation along the CIs, which replaces the θ'/Al-matrix interface with a C-θ'/$L1_2$ interface. The C-θ'/$L1_2$ interface has an almost zero interfacial energy unlike that of the C-θ'/Al-matrix interface (~200 mJ/m^2), and therefore, the driving force for Mn segregation is eliminated (more details can be found in Supplementary Fig. 2) [6, 8].

Cu, Mn, Zr, and Si 2D contour plots (2DCPs) reveal the solute segregation behaviors at the CIs and SCIs (Fig. 4). There are significantly higher Zr contents on the θ'-CIs for AM-ACMZ for similar aging conditions as cast-ACMZ consistent with the proximity histograms shown in Fig. 3. In fact, AM-ACMZ shows more interfacial Zr segregation after 9h at 350°C than cast-ACMZ after 200h at 350°C. The Si segregation behavior is similar between AM and cast-ACMZ. For all displayed heat treatments (9h, 350°C is the maximum AM-ACMZ exposure), Mn segregates to both the CIs and SCIs with more segregation to the SC interface. Only θ'-CIs were captured for a 220h, 350°C exposure for AM-ACMZ and did not show Mn segregation (Fig. 3), consistent with previously published results showing the same evolution of the Mn segregation behavior within cast-ACMZ after longer 350°C exposures [6]. Mn segregates to the C and SC interfaces in the early stages of thermal exposure. After extended thermal exposure at 350°C (>1,000h), Mn no longer segregates to θ'-SCIs and only segregates to some θ'-CIs. Therefore, it is safe to assume Mn is not segregating to θ'-SCIs after a 220h, 350°C exposure for AM-ACMZ. Overall, more Zr segregates to θ'-CIs and Mn ceases to segregate to all θ' interfaces after a shorter exposure to 350°C for AM-ACMZ compared to cast-ACMZ, which is expected to positively and negatively affect the thermal stability of θ' precipitates, respectively.

Discussion

Zr matrix content and interfacial segregation rate

One unique aspect of AM-ACMZ is that the matrix Zr content in the as-printed state is much higher than what can be achieved during casting due to rapid solidification conditions [23–26]. To understand the θ'-CI Zr segregation rate, the Zr Gibbsian Excess (GE) was calculated for over 50 θ'-CIs and 10 heat-treatment conditions using the method described by Krakauer and Seidman [6, 35, 36], and plotted against the Zr diffusion distance for the alloy's temperature/time exposure (shown in Fig. 5a). An example GE calculation and a detailed description can be found in Supplementary Fig. 5. The matrix Zr content vs. the Zr diffusion distance is plotted in Fig. 5b. The data in Fig. 5a were fit with linear functions, and the slopes represent the interfacial Zr segregation rate.

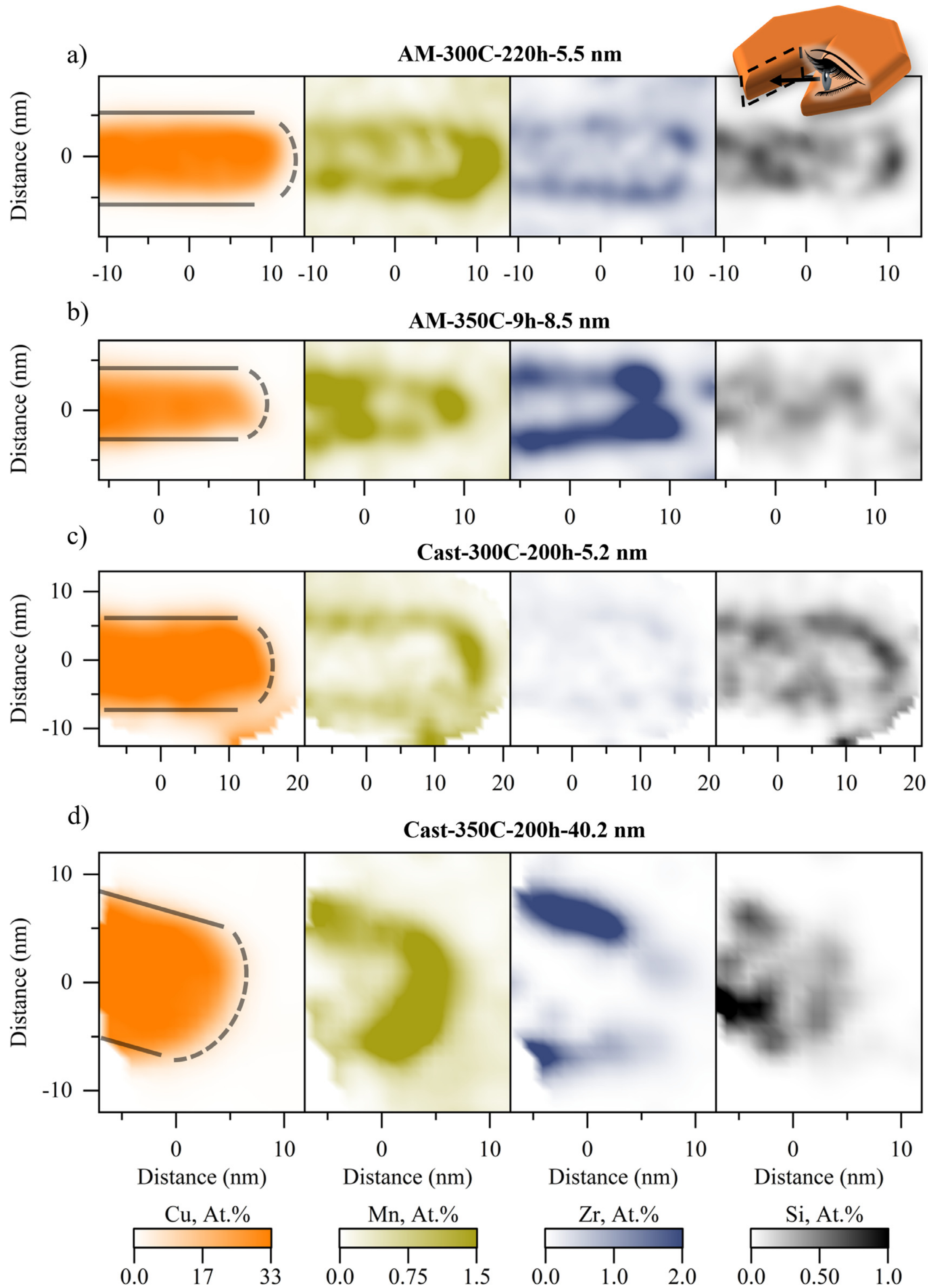

Fig. 4. Cross-sectional θ' 2DCPs of (a) AM-ACMZ after 300°C, 220h, (b) AM-ACMZ after 350°C, 9h, (c) cast-ACMZ after 300°C, 200h, and (d) cast-ACMZ after 350°C, 200h heat treatments. The solid and dashed lines in the Cu plots highlight the C and SC interfaces, respectively. The schematic in (a) shows the viewing direction for the 2DCPs. The displayed distances in the graph titles are the diffusion distances calculated using the method described in the caption of Table 2. Additional 2DCPs can be found in Supplementary Fig. 4.

The slopes for the cast-ACMZ are similar regardless of the exposure temperature with slopes of 0.04 and 0.02 for the 300 and 350°C heat treatments, respectively. On the other hand, the AM-300C slope data is ~5x larger than that of AM-350C, meaning that Zr segregates to θ'-CIs 5x faster when Zr diffuses up to ~10 nm than for when Zr diffuses ≳10 nm in AM-ACMZ. Interestingly, after Zr diffuses ≳10 nm, the θ'-CI Zr segregation rate matches that for cast-ACMZ. The differences and similarities in the slopes can be linked to the matrix Zr content (Fig. 5b).

The matrix Zr content is supersaturated for the first two AM-300C points (0 nm (as-printed) and 5.5 nm) with 15x and 5x more Zr than

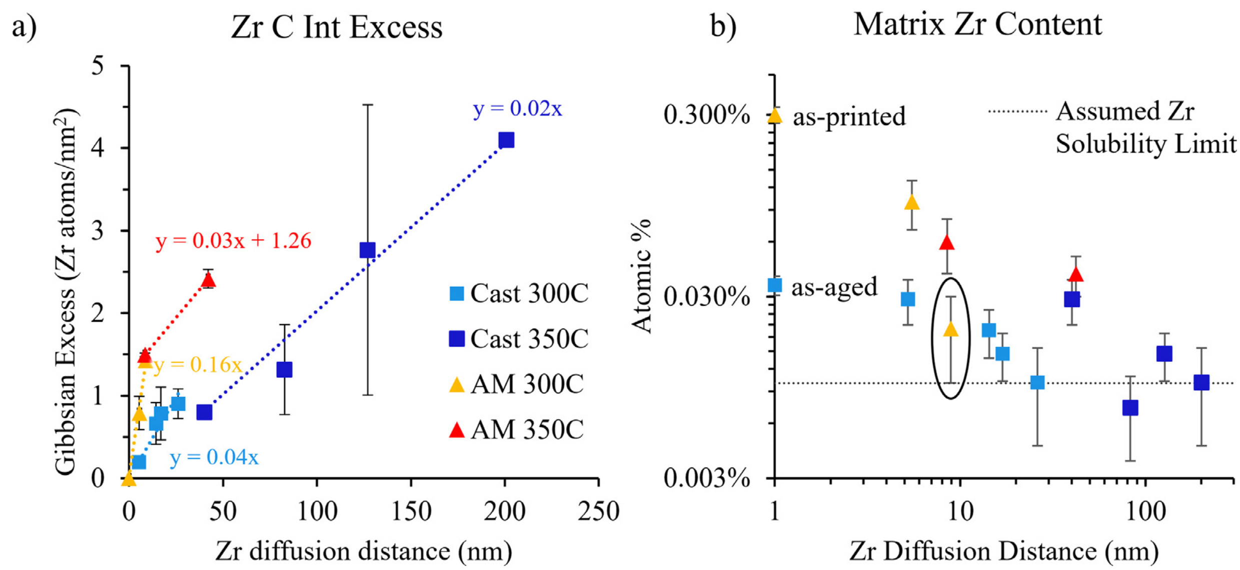

Fig. 5. (a) The θ'-CI excess plotted against the Zr diffusion distance for over 10 heat treatment conditions. The plotted values are the weighted average GE for several θ'-CIs, and the error bars are the standard deviation. The individual interface GE values can be found in Supplementary Tables 1 and 2 and the plotted data points can be found in Supplementary Tables 2 and 3. The slopes are the rate Zr segregates to θ'-CIs. All y-intercepts were set to 0 except for the AM-350°C data points because of the change in slope after the matrix Zr content stabilizes. (b) The matrix Zr content vs. the Zr diffusion distance. The circled AM-ACMZ points show the Zr diffusion distance required for the matrix Zr content to equal that of cast-ACMZ. The stable Zr content is plotted as a straight dotted line based on the stable matrix Zr content after >200h, 350°C exposures (The Zr solubility limit has been calculated as approximately 0.001 at. % at 350°C according to Clouet *et al.*) [37]. The diffusion distances were calculated using the method described in the caption of Table 2. The Mn θ'-CI excess data is displayed in Supplementary Fig. 2. The increase in matrix Zr content for the first cast-ACMZ 350°C data point is most likely due to a problem with the diffusion distance calculation for 300°C vs. 350°C in which the error in the calculated diffusion distance is not linear with temperature for this system.

after Zr diffuses ≳10 nm, respectively. The AM-ACMZ Zr matrix content matches that of cast-ACMZ after Zr diffuses ≳10 nm (circled point in Fig. 5b), pointing to the fact that the driving force for Zr to come out of the matrix when it is supersaturated is extremely high. This observation explains the rapid spherical $L1_2$ precipitation (spaced approximately 20 nm apart) and $L1_2/\theta$'-CI co-precipitation for AM-ACMZ as Zr diffuses up to ~10 nm. $L1_2/\theta$'-CI co-precipitation has only been scarcely observed using HAADF-STEM imaging in cast-ACMZ when Zr diffuses >40 nm (350°C, 200h) as the driving force for Zr to come out of the cast matrix is lower than that of a supersaturated matrix (AM-ACMZ). Overall, the rate Zr segregates to θ'-CIs is directly proportional to the Zr matrix concentration, and therefore, $L1_2/\theta$'-CI co-precipitation occurs much faster in AM-ACMZ than cast-ACMZ.

Continuous Zr Segregation to θ' interfaces

Interestingly, Zr continues to segregate to θ'-CIs after the matrix Zr content stabilizes as shown in Fig. 5 after >20 nm Zr diffusion distances (maximum exposure is 5,000h at 350°C). We note that the (Al_3Zr)-$L1_2/\theta$'-CI is a unique metallurgical feature where the tendency for Zr to segregate does not change with time because the (Al_3Zr)-$L1_2/\theta$' interface has a near 0 interfacial energy making θ'-CIs near-perfect templates for Zr segregation and subsequent (Al_3Zr)-$L1_2$ formation [6]. As such, the Zr segregation thermodynamics remain nearly constant due to several unique events: (a) there is a deep energy well for Zr solutes near the coherent interface and (b) as soon as a Zr atom fills an energy well, a new energy well with the same depth is automatically created because the second nearest neighbor is available for $L1_2$ structure formation. These unique aspects regarding the solute segregation thermodynamics on the (Al_3Zr)-$L1_2/\theta$'-CI means the Zr segregation rate to the θ'-CIs (the slopes in Fig. 5a) simply reflects the Zr concentration in the nearby matrix. Zr will continue to segregate if given enough kinetic opportunity, i.e. time and temperature, and the Zr matrix content remains above equilibrium (calculated as approximately 0.001 at. % at 350°C) [37].

θ' templates for planar L12 formation

The way θ' disappears in AM-ACMZ is unique in that it does not appear to coarsen and transform into θ, rather the θ'-CIs are locked by the $L1_2$ precipitates, and Cu dissolves out of θ' into the matrix (see Fig. 1f and Supplementary Fig. 1). Interestingly, stable planar $L1_2$ precipitates remain where they previously formed on θ'-CIs, which provides strength. A schematic of this phenomenon is shown in Fig. 6. Overall, θ' is a template that forms stable planar Al_3Zr-$L1_2$ precipitates instead of their typical spherical shape that can provide a separate strengthening mechanism for this alloy at higher temperatures [27]. This work introduces the idea that metastable precipitates with unique interfacial properties can be used to attract slower diffusing solutes that form a unique and desirable stable precipitate geometry. The high solute matrix contents introduced by AM processing can expediate the stable precipitate growth rate. This concept can be used to improve the thermal stability of Al-Cu alloys as well as other high strength alloys.

Conclusions

The solute segregation behavior to θ' interfaces was studied for cast and AM-ACMZ alloys with a primary focus on interfacial Zr segregation and planar $L1_2$ formation. The Zr segregation rate to θ'-CIs was found to be directly proportional to the matrix Zr content, exhibiting unique metallurgical properties. The near zero interfacial energy makes θ'-CIs perfect templates for Al_3Zr-$L1_2$ formation, and Zr continues to segregate to θ'-CIs after extensive over-aging. The supersaturated Zr matrix facilitated by rapid cooling during AM allows for faster Al_3Zr-$L1_2/\theta$' co-precipitate formation than cast ACMZ. SS S Stable planar $L1_2$ precipitates remain after θ' dissolves providing strength at higher temperatures. Overall, the nature of the θ'-CI is unique in that it can accept continuous Zr segregation and is a perfect template to form a desired planar $L1_2$ geometry. These results suggest that designing an AM θ' strengthened Al alloy with a supersaturated Zr matrix content and a high θ' precipitate density spaced >20 nm apart would produce a microstruc-

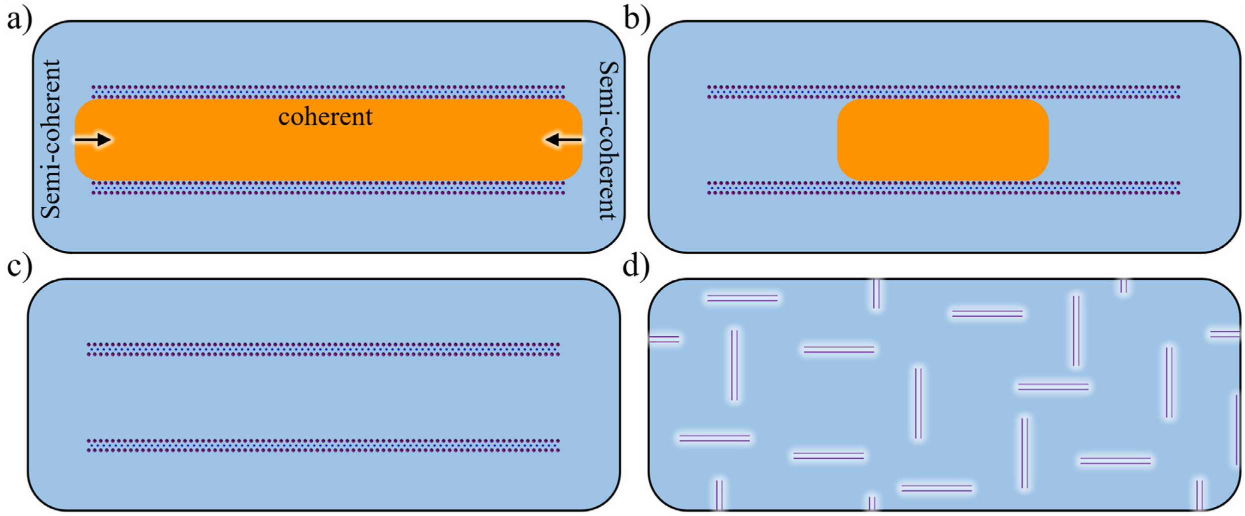

Fig. 6. A schematic of θ' dissolution after $L1_2$ precipitation locks the CIs leaving behind planar $L1_2$ precipitates in the α-Al matrix. This shows how metastable θ' precipitates are a template for forming stable planar $L1_2$ strengthening precipitates in Al. a) An $L1_2/\theta$' co-precipitate within the α-Al matrix. b) The θ' CIs are locked by the $L1_2$ precipitation, while the SCIs close in on each other as Cu dissolves from the precipitates during high temperature exposure. c) Planar $L1_2$ precipitates remain after θ' dissolution where they previously precipitated on θ' CIs. d) The α-Al matrix is littered with residual planar $L1_2$ precipitates after θ' dissolution providing strength to the material.

ture littered with stable planar $L1_2$ that would retain its strength for lengthier exposures than cast Al-Cu alloys. Additionally, the concept of using metastable precipitates as templates to form another desired stable precipitate geometry can be used to improve the thermal stability of any alloy system containing precipitates with analogous interfacial characteristics.

Declaration of Competing Interest

The authors have no conflicts of interests to declare.

Acknowledgments

This research was supported by the DOE Office of Energy Efficiency and Renewable Energy, Vehicle Technologies Office, Propulsion Materials Program and the Advanced Manufacturing Office. APT research was supported by the Center for Nanophase Materials Sciences (CNMS), which is a US Department of Energy, Office of Science User Facility at Oak Ridge National Laboratory. The authors would like to thank James Burns for assistance in performing APT sample preparation and running the APT experiments. The authors would also like to thank Dana McClurg for heat treatments, and Brian Eckhart and Travis Dixon for thin-foil preparation for electron microscopy.

Supplementary materials

Supplementary material associated with this article can be found, in the online version, at doi:10.1016/j.addlet.2022.100086.

References

[1] S. Roy, L.F. Allard, A. Rodriguez, W.D. Porter, A. Shyam, Comparative evaluation of cast aluminum alloys for automotive cylinder heads: part II—mechanical and thermal properties, Metall. Mater. Trans. A 48 (5) (2017) 2543–2562.
[2] S. Roy, L.F. Allard, A. Rodriguez, T.R. Watkins, A. Shyam, Comparative evaluation of cast aluminum alloys for automotive cylinder heads: part I—microstructure evolution, Metall. Mater. Trans. A 48 (5) (2017) 2529–2542.
[3] M. Javidani, D. Larouche, Application of cast Al–Si alloys in internal combustion engine components, Int. Mater. Rev. 59 (3) (2014) 132–158.
[4] A. Shyam, S. Roy, D. Shin, J.D. Poplawsky, L.F. Allard, Y. Yamamoto, J.R. Morris, B. Mazumder, J.C. Idrobo, A. Rodriguez, T.R. Watkins, J.A. Haynes, Elevated temperature microstructural stability in cast AlCuMnZr alloys through solute segregation, Mater. Sci. Eng., A (2019) 138279.
[5] J. Ding, C. Cui, Y. Sun, L. Zhao, S. Cui, Effect of Mo, Zr, and Y on the high-temperature properties of Al–Cu–Mn alloy, J. Mater. Res. 34 (22) (2019) 3853–3861.
[6] J.D. Poplawsky, B.K. Milligan, L.F. Allard, D. Shin, P. Shower, M.F. Chisholm, A. Shyam, The synergistic role of Mn and Zr/Ti in producing θ'/L12 co-precipitates in Al-Cu alloys, Acta Mater 194 (2020) 577–586.
[7] S. Liu, E. Martínez, J. Llorca, Prediction of the Al-rich part of the Al-Cu phase diagram using cluster expansion and statistical mechanics, Acta Mater. 195 (2020) 317–326.
[8] V. Vaithyanathan, C. Wolverton, L.Q. Chen, Multiscale modeling of θ' precipitation in Al–Cu binary alloys, Acta Mater. 52 (10) (2004) 2973–2987.
[9] Y.H. Gao, L.F. Cao, C. Yang, J.Y. Zhang, G. Liu, J. Sun, Co-stabilization of θ'-Al2Cu and Al3Sc precipitates in Sc-microalloyed Al-Cu alloy with enhanced creep-resistance, Mater. Today Nano (2019) 100035.
[10] P. Shower, J. Morris, D. Shin, B. Radhakrishnan, J. Poplawsky, A. Shyam, Mechanisms for stabilizing θ'(Al2Cu) precipitates at elevated temperatures investigated with phase field modeling, Materialia 6 (2019) 100335.
[11] Y.H. Gao, L.F. Cao, J. Kuang, J.Y. Zhang, G. Liu, J. Sun, Assembling dual precipitates to improve high-temperature resistance of multi-microalloyed Al–Cu alloys, J. Alloys Compd. (2020) 153629.
[12] Y.H. Gao, C. Yang, J.Y. Zhang, L.F. Cao, G. Liu, J. Sun, E. Ma, Stabilizing nanoprecipitates in Al-Cu alloys for creep resistance at 300°C, Mater. Res. Lett. 7 (1) (2018) 1–9.
[13] L. Jiang, B. Rouxel, T. Langan, T. Dorin, Coupled segregation mechanisms of Sc, Zr and Mn at θ' interfaces enhances the strength and thermal stability of Al-Cu alloys, Acta Mater. 206 (2021) 116634.
[14] A. Tolley, V. Radmilovic, U. Dahmen, Segregation in Al3(Sc,Zr) precipitates in Al–Sc–Zr alloys, Scr. Mater. 52 (7) (2005) 621–625.
[15] V. Radmilovic, C. Ophus, E.A. Marquis, M.D. Rossell, A. Tolley, A. Gautam, M. Asta, U. Dahmen, Highly monodisperse core–shell particles created by solid-state reactions, Nat. Mater. 10 (9) (2011) 710–715.
[16] E. Clouet, L. Laé, T. Épicier, W. Lefebvre, M. Nastar, A. Deschamps, Complex precipitation pathways in multicomponent alloys, Nat. Mater. 5 (6) (2006) 482–488.
[17] J. Zhang, B. Wang, H. Wang, C. Zhang, Improvement in compressive creep resistance of Al-0.2Zr alloy with L12 structured Sc-enriched precipitates, Mater. Charact. 159 (2020) 110024.
[18] R. Shi, D.P. McAllister, N. Zhou, A.J. Detor, R. DiDomizio, M.J. Mills, Y. Wang, Growth behavior of γ'/γ'' coprecipitates in Ni-Base superalloys, Acta Mater 164 (2019) 220–236.
[19] K.E. Knipling, D.C. Dunand, D.N. Seidman, Criteria for developing castable, creep--resistant aluminum-based alloys – A review, Z. Metallk. 97 (3) (2006) 246–265.
[20] G. Rummel, T. Zumkley, M. Eggersmann, K. Freitag, H. Mehrer, Diffusion of implanted 3d-transition elements in aluminium. Part I: temperature dependence, Z. Metallk. 86 (2) (1995) 122–130.
[21] T. Marumo, S. Fujikawa, K. Hirano, Diffusion of zirconium in aluminum, J. Jpn. Insti. Light Metal. 23 (17) (1973).
[22] A. Shyam, A. Plotkowski, S. Bahl, K. Sisco, L.F. Allard, Y. Yang, J.A. Haynes, R.R. Dehoff, An additively manufactured AlCuMnZr alloy microstructure and tensile mechanical properties, Materialia 12 (2020) 100758.
[23] S. Griffiths, M.D. Rossell, J. Croteau, N.Q. Vo, D.C. Dunand, C. Leinenbach, Effect of laser rescanning on the grain microstructure of a selective laser melted Al-Mg-Zr alloy, Mater. Charact. 143 (2018) 34–42.
[24] J.R. Croteau, S. Griffiths, M.D. Rossell, C. Leinenbach, C. Kenel, V. Jansen, D.N. Sei-

dman, D.C. Dunand, N.Q. Vo, Microstructure and mechanical properties of Al-Mg-Zr alloys processed by selective laser melting, Acta Mater. 153 (2018) 35–44.

[25] K.E. Knipling, D.C. Dunand, D.N. Seidman, Nucleation and precipitation strengthening in dilute Al-Ti and Al-Zr alloys, Metall. Mater. Trans. A 38 (10) (2007) 2552–2563.

[26] J. Murray, A. Peruzzi, J.P. Abriata, The Al-Zr (aluminum-zirconium) system, J. Phase Equilib. 13 (3) (1992) 277–291.

[27] R.A. Michi, K. Sisco, S. Bahl, L.F. Allard, K.B. Wagner, J.D. Poplawsky, D.N. Leonard, R.R. Dehoff, A. Plotkowski, A. Shyam, Microstructural evolution and strengthening mechanisms in a heat-treated additively manufactured Al–Cu–Mn–Zr alloy, Mater. Sci. Eng. 840 (2022) 142928.

[28] S. Bahl, L. Xiong, L.F. Allard, R.A. Michi, J.D. Poplawsky, A.C. Chuang, D. Singh, T.R. Watkins, D. Shin, J.A. Haynes, A. Shyam, Aging behavior and strengthening mechanisms of coarsening resistant metastable θ' precipitates in an Al–Cu alloy, Mater. Des. 198 (2021) 109378.

[29] X. Hu, S. Bahl, A. Shyam, A. Plotkowski, B. Milligan, L. Allard, J. Haynes, Y. Ren, A. Chuang, Repurposing the Al_2Cu phase to simultaneously increase the strength and ductility of an additively manufactured Al-Cu alloy, Mater. Sci. Eng 850 (2022) 143511.

[30] R.A. Michi, A. Plotkowski, A. Shyam, R.R. Dehoff, S.S. Babu, Towards high-temperature applications of aluminium alloys enabled by additive manufacturing, Int. Mater. Rev. 67 (3) (2022) 298–345.

[31] K. Thompson, D. Lawrence, D.J. Larson, J.D. Olson, T.F. Kelly, B. Gorman, In situ site-specific specimen preparation for atom probe tomography, Ultramicroscopy 107 (2-3) (2007) 131–139.

[32] P. Shower, J. Poplawsky, S. Bahl, A. Shyam, The role of Si in determining the stability of the θ' precipitate in Al-Cu-Mn-Zr alloys, J. Alloys Compd. 862 (2021) 158152.

[33] B.K. Milligan, S. Roy, C.S. Hawkins, L.F. Allard, A. Shyam, Impact of microstructural stability on the creep behavior of cast Al–Cu alloys, Mater. Sci. Eng. 772 (2020) 138697.

[34] J.U. Rakhmonov, S. Bahl, A. Shyam, D.C. Dunand, Cavitation-resistant intergranular precipitates enhance creep performance of θ'-strengthened Al-Cu based alloys, Acta Mater. 228 (2022) 117788.

[35] B.W. Krakauer, D.N. Seidman, Absolute atomic-scale measurements of the Gibbsian interfacial excess of solute at internal interfaces, Phys. Rev. B 48 (9) (1993) 6724–6727.

[36] Y.J. Li, D. Ponge, P. Choi, D. Raabe, Atomic scale investigation of non-equilibrium segregation of boron in a quenched Mo-free martensitic steel, Ultramicroscopy 159 (2015) 240–247.

[37] E. Clouet, J.M. Sanchez, C. Sigli, First-principles study of the solubility of Zr in Al, Phys. Rev. B 65 (9) (2002) 094105.